ACCELERATED-SCAN X-RAY MICROTOMOGRAPHY FOR ASSESSING BONE MINERAL CONTENT

PURISHA Z, KARHULA SS, KETOLA J, RIMPELÄINEN J, NIEMINEN MT, SAARAKKALA S AND SILTANEN S

Abstract. X-ray tomography is a reliable tool for determining density and three-dimensional (3D) structure of bone tissue. However, traditional reconstruction methods such as FDK require dense angular sampling in data acquisition phase leading to long measurement times. Especially in X-ray micro-tomography acquisition times between 6 and 12 hours are typical in high-resolution scans. Acquiring less data using greater angular steps is an obvious way for speeding up the process. However, computing 3D reconstruction from such a sparsely sampled dataset is very sensitive to measurement noise and modelling errors. An automatic regularization method is proposed for robust reconstruction, based on enforcing sparsity in the three-dimensional shearlet transform domain. The inputs of the algorithm are the projection data and *a priori* known expected degree of sparsity, denoted $0 < \mathcal{C}_{pr} \leq 1$. The number $\mathcal{C}_{pr}$ can be calibrated from a few dense-angle reconstructions and fixed. The morphology of the bone is then analyzed using standard metrics. The proposed method is shown to outperform the baseline algorithm (FDK) in the case of sparsely collected data. The number of X-ray projections can be reduced to 10% of the currently used amount while retaining quality of morphology analysis.

1. Introduction

Bone morphology studies using X-ray micro-tomography (μCT) have recently gained importance in biomedical research. In μCT one rotates a bone sample in an X-ray cone-beam and collects a set of projection images from many directions. A mathematical reconstruction algorithm is used for revealing three-dimensional (3D) density structure inside the sample. Various bone quality metrics can then be applied to the resulting digital 3D volume.

Traditional reconstruction methods such as Feldkamp-Davis-Kress type (FDK) [1] require densely sampled datasets for achieving sufficient reconstruction quality. More precisely, denote the projection angles by $\theta, 2\theta, \ldots, N\theta = 180$, with a fixed angular step $\theta > 0$. The FDK algorithm typically needs $N > 500$ for delivering a high enough reconstruction quality. This often leads to impractically long measurement times, especially in μCT where acquisition times between 6 and 12 hours are typical in high-resolution scans. Moreover, in longitudinal *in vivo* animal studies the cumulative radiation dose can modify the properties of living tissue, thereby biasing the results [2].

A simple way to speed up the acquisition process and reduce the radiation dose is to collect less data by decreasing N and enlarging the angular step θ accordingly so that the 180 degree half-circle is still sampled. However, the task of computing a 3D reconstruction from such a sparsely sampled dataset becomes extremely sensitive to modelling errors and measurement noise. In mathematical terms, it is an *ill-posed inverse problem* [3] that needs to be regularized by making use of *a priori* information about the bone structure.

In this work, we investigate the reliability of a modern sparsity-promoting 3D reconstruction algorithm for assessing bone morphology using sparse X-ray tomographic data. We concentrate on human trabecular bone structures [4, 5, 6, 7].

We quantify bone morphology using four standard parameters calculated from 3D reconstructions:

- the percentage of bone volume (BV/TV),
- the mean thickness of trabeculae ($Tb.Th$),
- the trabecular number ($Tb.N$), and
- the mean distance between trabeculae ($Tb.Sp$).

These parameters are important descriptors of bone tissue health. They reveal the changes in the 3D structure of bone caused by osteoarthritis [8, 9] or subchondral bone sclerosis [10, 11]. We use Computed Tomography Analyzer (CTAn) software for calculating bone morphometric parameters. The parameters are defined for binary (bone/not-bone) 3D reconstructions; we use the Otsu algorithm in CTAn for segmentation [12].

The *shearlet transform* is a tool for orientation-aware multiscale signal processing [13, 14]. Shearlets provide efficient representations for a variety of signals, see for example [15]. We implement a 3D tomographic reconstruction algorithm regularized by promoting sparsity of the bone structure in the shearlet transform domain. We use iterative

soft thresholding algorithm (ISTA) as outlined in [16]. The method was one of the earliest introduced in [17].

We introduce a novel technique for making the regularized reconstruction process fully automatic. Namely, the ISTA method involves a thresholding parameter $\mu > 0$. All shearlet coefficients smaller than $\frac{\mu}{2}$ in absolute value are set to zero in each iteration. How to choose a suitable value for μ?

If μ is large, then many coefficients vanish and the reconstruction is very sparse in the shearlet domain. If μ is small, then almost all shearlet coefficients of the final reconstruction will be nonzero. We propose determining the typical ratio $0 < \mathcal{C}_{pr} \leq 1$ of nonzero shearlet coefficients from a few dense-angle 3D reconstructions of both healthy and osteoarthritic bone samples. We let $\mu = \mu_j$ change in each iteration and apply a simple control algorithm so that μ_j converges to a limit value producing a reconstruction having the *a priori* known sparsity $\mathcal{C}_{pr}$. The integral controller, part of proportionalintegralderivative controller (PID controller), is implemented in this approach [18].

The reconstructions using 3D shearlet-sparsity regularization is shown to outperform FDK in the case of sparsely collected data. With the shearlet-sparsity reconstruction method, the number of X-ray projections can be reduced to 10% of the currently used amount while retaining the quality of morphology analysis.

Shearlet-based methods for X-ray tomography have been studied before, starting with [19] concentrating on inversion from noisy, densely sampled 2D sinograms. Total variation regularization and shearlet sparsity are successfully combined for 2D tomographic data in [20, 21], including sparse data with a minimum of 128 angles. Shearlets are shown to be useful for 2D region-of-interest tomography in [22] and for limited-angle tomography in [23].

A study to recover bone structure in 2D from sparse microtomography data using a tomographic method called discrete algebraic reconstruction technique (DART) was introduced [24, 25]. However, the method proposed here is based on different assumptions about *a priori* knowledge. DART needs rather accurate attenuation value estimates as input and assumes that the target consists of a small number of possible materials.

Regarding 3D tomography, the only shearlet study seems to be [26] showing the optimality for representing tomographic data in terms of shearlets. To our best knowledge, the present work is the first application of the 3D shearlet transform to measured X-ray tomographic data.

2. Materials and Methods

2.1. **3D Tomographic Setup.** The goal of X-ray tomography is to recover the density function of an unknown object from measured projection data. In this paper, the object is three-dimensional, and cone-beam geometry is used for modeling the measurement.

Consider a physical domain $\Omega \subset \mathbb{R}^3$ and a non-negative X-ray attenuation function $f : \Omega \to \mathbb{R}$. The X-rays travel through Ω along straight lines $L \subset \Omega$. After calibration, each pixel value in the collection of digital radiographs yields a line integral $\int_L f(x)ds$.

For computational reasons, a discrete model is required. Let us represent the attenuation values by a vector $\mathbf{f} = [\mathbf{f}_{ijk}] \in \mathbb{R}^{N\times N\times T}$. Here $\mathbf{f}_{ijk}$ denotes the average of the values of the function f over the voxel with indices (i, j, k).

The line integral can be approximated by

$$\int_L f(x)ds \approx \sum_{i=1}^{N}\sum_{j=1}^{N}\sum_{k=1}^{T} a_{ijk}\mathbf{f}_{ijk}, \tag{1}$$

where a_{ijk} is a distance that the line L travels in the voxel with indices (i, j, k). Then the practical three-dimensional tomographic X-ray data is modeled by

$$\mathbf{m} = \mathbf{A}\mathbf{f}, \tag{2}$$

with a matrix $\mathbf{A}$ containing one row for each pixel in the set of measurements.

We use the normalized measurement matrix $\frac{\mathbf{A}}{\|\mathbf{A}\|}$ and measurement data $\frac{\mathbf{m}}{\|\mathbf{A}\|}$. Note that the norm of $\mathbf{A}$ equals $\sqrt{\lambda}$, where λ is the largest eigenvalue of the symmetric matrix $\mathbf{A}^T\mathbf{A}$. The power method can be used to compute λ in a matrix-free fashion [27]. Multiplication by the matrices $\mathbf{A}$ and $\mathbf{A}^T$ can be implemented by using the SPOT operator [28].

2.2. **The Shearlet Transform.** Shearlets form a directional representation system for multidimensional data [29, 30]. They can overcome limitations of traditional systems like wavelets that only provide optimally sparse representations for functions of one variable. In the 3D case, shearlets offer optimal approximation of piecewise smooth functions with jumps appearing only along smooth surfaces.

Shearlets are parameterized by scale, shearing and translation indices organized in the set

$$\Lambda = \mathbb{N}_0 \times \{\lceil -2^{j/2}\rceil, \ldots, \lceil 2^{j/2}\rceil\} \times \mathbb{Z}^3.$$

It has been shown in [13] that, under suitable assumptions, the collection $\psi_\gamma = \psi_{(l,m,n)} \in L^2(\mathbb{R}^3)$, where $\gamma = (l, m, n) \in \Lambda$, forms a *frame* for $L^2(\mathbb{R}^3)$ functions. The shearlet transform is defined as the following vector of coefficients:

$$\mathcal{S}(\mathbf{f}) = (\langle \mathbf{f}, \psi_\gamma \rangle)_{\gamma \in \Lambda}. \tag{3}$$

We use the ShearLab implementation [14].

2.3. **Sparsity-promoting regularization.** In this work, we are interested in finding the vector $\mathbf{f}$ that minimizes the variational regularization functional

$$\|\mathbf{Af} - \mathbf{m}\|_2^2 + \mu \sum_\gamma |\langle \mathbf{f}, \psi_\gamma \rangle|. \tag{4}$$

The parameter μ in (4) describes a trade-off between emphasizing either the data fidelity term or the regularizing penalty term more.

We introduce a regularization method based on enforcing sparsity in the shearlet transform domain. We apply ISTA method introduced in [16] in the form

$$\begin{cases} \mathbf{g}^{(n+1)} & = \mathbf{f}^{(n)} + \mathbf{A}^T(\mathbf{m} - \mathbf{Af}^{(n)}) \\ \mathbf{w}^{(n+1)} & = P_\mu \left(\mathbf{w}^{(n)} + \mathcal{S}(\mathbf{g}^{(n+1)} - \mathcal{S}^T \mathbf{w}^{(n)}) \right) \\ \mathbf{f}^{(n+1)} & = \mathbf{g}^{(n+1)} - \mathcal{S}^T \mathbf{w}^{(n+1)}, \end{cases} \tag{5}$$

where $\mathcal{S}^T$ is the adjoint of shearlet transform, $P_\mu = Id - \mathcal{T}_\mu$ and $\mathcal{T}_\mu$ denotes element-wise application of the soft-thresholding function

$$\mathcal{T}_\mu(c) = \begin{cases} c + \frac{\mu}{2} & \text{if } c \leq -\frac{\mu}{2} \\ 0 & \text{if } |c| < \frac{\mu}{2} \\ c - \frac{\mu}{2} & \text{if } c \geq -\frac{\mu}{2}. \end{cases} \tag{6}$$

Here $\mu \geq 0$ is a thresholding parameter. Also, we enforce non-negativity of the X-ray attenuation coefficient by replacing any negative pixels in $\mathbf{f}^{(i)}$ by zeros in each iteration.

2.4. **Automatic Selection of the Threshold Parameter μ.** Assume that we know *a priori* the expected degree of sparsity in the reconstruction, denoted $0 < \mathcal{C}_{pr} \leq 1$. We use a simple feedback control system for finding such a value of μ that the iteration (5) produces a result with exactly $\mathcal{C}_{pr} \cdot 100\%$ of its shearlet coefficients nonzero.

In our proposed method, $\mu = \mu^{(i)}$ is allowed to vary during the iteration. Furthermore, it is automatically tuned in every iteration:

$$\mu^{(i+1)} := \mu^{(i)} + \beta e^{(i+1)},$$

where $e^{(i+1)} = \mathcal{C}^{(i)} - \mathcal{C}_{pr}$ and $0 \leq \mathcal{C}^{(i)} \leq 1$ is the sparsity level of the current iterate $\mathbf{f}^{(i)}$. To avoid slow convergence, the stepsize $\beta > 0$ cannot be too small and to address this we choose large beta but decrease it each time the sparsity level crosses the desired level of sparsity:

$$\beta = \beta(1 - |e^{(i+1)} - e^{(i)}|).$$

This approach can avoid unwanted oscillation in the values $\mu^{(i)}$.

2.5. **Bone Quality Measures.** We study human trabecular bone samples. Reccommended parameters to study the 3D structure of bone [8] include:

(1) Percentage of bone volume (BV/TV). BV refers to volume of the region segmented as bone and BV/TV refers to ratio of the segmented bone volume to the total volume of the region of interest (ROI).
(2) Trabecular thickness ($Tb.Th$): mean thickness of trabeculae (μm)
(3) Trabeculae number ($Tb.N$): measure of the average number of trabecular per unit length ($\frac{1}{\mu m}$)
(4) Trabecular separation ($Tb.Sp$): mean distance between trabeculae (μm)

To calculate the basic bone morphometric parameters, a standard Computed Tomography Analyzer (CTAn) software provided by the manufacturer (Bruker microCT, Kontich, Belgium) was used. The reconstructed images were converted to 8 bit images and then segmented into binary images for morphology analysis in CTAn. Because the samples were drilled from bone, physical artifacts such as bone dust or cracks were left from the preparation. Therefore, a region of interest (ROI) inside the sample was selected so that the edge artifacts will not affect the analysis.

2.6. **Determining the *A Priori* Degree of Sparsity.** Let us denote the sparsity level $\mathcal{C}$ as the number of nonzero elements of $\mathcal{T}_\mu(c)$. The *a priori* sparsity level value $\mathcal{C}_{pr}$ was estimated using FDK reconstruction of the bone from the full set projection images. Later we call the full reconstruction image as a ground truth and denote it as G.

The calculation of the sparsity prior is given as follows.

(1) The coefficients were collected by applying shearlet transform to the ground truth,

$$\mathscr{S}_G = \mathcal{S}(G).$$

(2) The coefficients $\mathscr{S}_G$ were sorted in ascending order and denote it as $\widetilde{\mathscr{S}_G}$ and hard-thresholded in different levels of sparsity,

$$\widetilde{\mathscr{S}_G}^{\widetilde{\mu}} = \widetilde{\mathcal{T}_{\widetilde{\mu}}}(\widetilde{\mathscr{S}_G}),$$

where

$$\widetilde{\mathcal{T}_{\widetilde{\mu}}}(c) = \begin{cases} c & \text{if } |c| \geq \widetilde{\mu}, \\ 0 & \text{if } |c| < \widetilde{\mu}. \end{cases} \tag{7}$$

The thresholded parameter $\widetilde{\mu}$ was selected so that the number of nonzero coefficients in $\widetilde{\mathscr{S}_G}^{\widetilde{\mu}}$ matched a particular degree of sparsity.

(3) The operator of the dual frame was applied to each $\widetilde{\mathscr{S}_G}^{\widetilde{\mu}}$:

$$\widetilde{G^{\widetilde{\mu}}} = \mathcal{S}^{\dagger}(\widetilde{\mathscr{S}_G}^{\widetilde{\mu}}).$$

(4) The bone quality parameters *BV/TV, Tb.Th, Tb.N* and *Tb.Sp* were calculated for each $\widetilde{G^{\widetilde{\mu}}}$.

2.7. **Pseudo-algorithm.** The algorithm we use is written as in **Algorithm 1**.

Algorithm 1 Shearlet sparsity-promoting tomographic reconstruction algorithm with automatic parameter choice method. Inputs are: measurement data vector $\mathbf{m}$, system matrix $\mathbf{A}$, *a priori* degree of sparsity $\mathcal{C}_{pr}$, initial thresholding parameter μ_0, maximum number of iterations I_0, tolerance $\epsilon > 0$ for the stopping rule, control stepsize $\beta > 0$.

$\mathbf{f}^0 = \mathbf{0}$, $i = 0$, $\mathcal{C}^{(0)} = 1$, and $e^{(0)} = \mathcal{C}^{(0)} - \mathcal{C}_{pr}$
while $i < I_0$ and $|e^{(i)}| \geq \epsilon$ **do**
  $e^{(i+1)} = \mathcal{C}^{(i)} - \mathcal{C}_{pr}$
  $\mu^{(i+1)} = \max\{0, \mu^{(i)} + \beta e^{(i+1)}\}$
  if $\text{sign}(e^{(i+1)}) \neq \text{sign}(^{(i)})$ **then**
    $\beta = \beta(1 - |e^{(i+1)} - e^{(i)}|)$
  $\mathbf{g}^{(i+1)} = \mathbf{f}^{(i)} + \mathbf{A}^T(\mathbf{m} - \mathbf{A}\mathbf{f}^{(i)})$
  $\mathbf{u} = \mathbf{w}^{(i)} + \mathcal{S}(\mathbf{g}^{(i+1)} - \mathcal{S}^T\mathbf{w}^{(i)})$
  $\mathbf{w}^{(i+1)} = \mathbf{u} - \mathcal{T}_{\mu^{(i)}}(\mathbf{u})$
  $\mathbf{f}^{(i+1)} = \mathbf{g}^{(i+1)} - \mathcal{S}^T\mathbf{w}^{(i+1)}$
  $\mathscr{S} = \mathcal{T}_{\mu^{(i)}}\left(\mathcal{S}(\mathbf{f}^{(i+1)})\right)$
  $\mathcal{C}^{(i+1)} = \#(c)$, where c is the nonzero coefficient of the shearlet coefficient $\mathscr{S}$.
  $\mathbf{f}^{(i+1)} = \max\{0, \mathbf{f}^{(i+1)}\}$
  i := i+1

TABLE 1. Total angle of view for each restricted set of projection images

Number of projections	Total angle of view
120	178.5°
60	177.0°
40	175.5°

3. Results

3.1. **Data Acquisition.** X-ray data from human bones were acquired. The core samples were drilled from tibial plateau and the corresponding femoral surface. The samples were osteochondral core with 4 mm diameter. The samples were harvested from the patient going through total knee replacement (ethical permission no. 78/2013, approved by ethical committee of Northern Ostrobothnia Hospital District). The X-ray tomography data was acquired with SkyScan 1272 high-resolution CT scanner (Bruker microCT, Kontich, Belgium). The isotropic voxel size length for projection 2.75 μm/pixel and the number of frames averaged is 2 per projection. A set of 596 projection images were acquired over a full 178.5 degree rotation with uniform angular step of 0.3 degrees between projections. Each projection image was composed of 3200 ms exposures. The X-ray tube acceleration voltage was 50 kV and tube current 200 μA, and the full polychromatic beam was used for image acquisition. The additional filtration was 0.5 mm of Aluminium.

We used 596 projections for ground truth reconstructions. We picked several subsets of projections (40, 60 and 120) from the measured data with uniform angular sampling from different total opening angles of each projection images. See Table 1.

3.2. **Bones Parameters Values using Different Sparsity Levels.** The ground truth G was computed using FDK method with full set 596 projection images. The reconstruction has a sized $N \times N \times T$ with $N = 256$ and $T = 100$. See Subsection 3.1.

To solve the problem in (4), the algorithm as discussed in Subsection 2.6 was implemented. This sparsity prior was calculated only from one sample of the healthy and osteoarthritic bones. For an empirical study, more samples are required.

The thresholded parameters $\widetilde{\mu}$ were selected so that 5% to 95% of the number of nonzero coefficients were obtained. The calculations of the healthy and osteoarthritic bone parameters can be seen in Figure 1 and Figure 2, respectively. The stable values are indicated by circles.

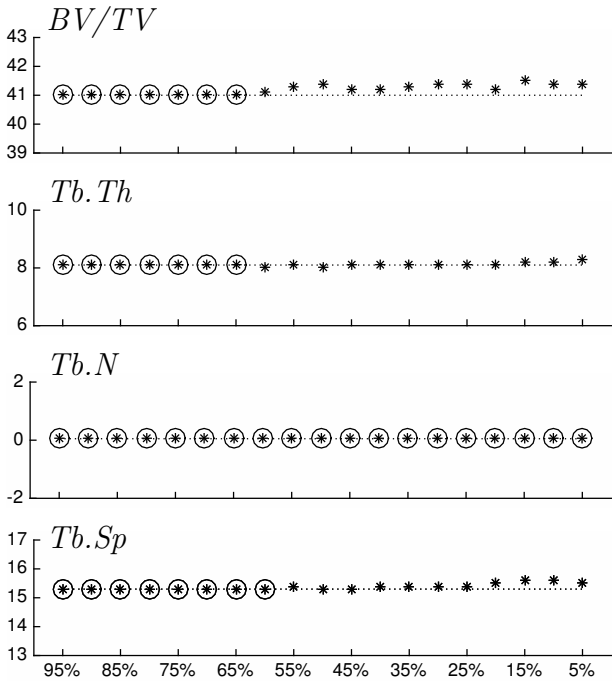

FIGURE 1. The value of bone parameters from inverse 3D shearlet transform of the healthy bone using different sparsity level as discussed in the step above. Stars with circles are the stable values.

The lowest number of nonzero coefficients that still yields the correct values for each of the four bone quality parameters was chosen and presented in Table 2 and Table 3.

The maximum value in Table 2 and Table 3 were chosen as the *a priori* degree of sparsity. Both the healthy and osteoarthritic result suggest the prior sparsity value

$$\mathcal{C}_{pr} = 65\%.$$

TABLE 2. The smallest percentage of nonzero coefficients that yield the same values of each osteoarthritic bone parameters. The stable values are indicated by circle in Figure 2.

Lowest sparsity level	*BV/TV*	*Tb.Th*	*Tb.N*	*Tb.Sp*
	65%	65%	5%	60%

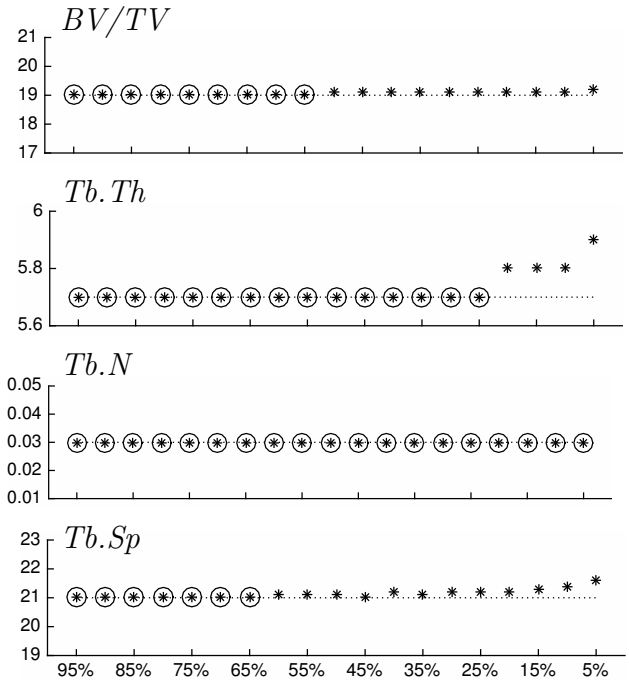

FIGURE 2. The value of bone parameters from inverse 3D shearlet transform of the osteoarthritic bone using different sparsity level as discussed in the step above. Stars with circles are the stable values.

TABLE 3. The smallest percentage of nonzero coefficients that yield the same values of each osteoarthritic bone parameters. The stable values are indicated by circle in Figure 2.

Lowest sparsity level	*BV/TV*	*Tb.Th*	*Tb.N*	*Tb.Sp*
	55%	65%	5%	25%

3.3. **Reconstructions.** For the reconstruction, we set a 3D image sized $N \times N \times T$ with $N = 256$ and $T = 100$. All the algorithms were implemented in Matlab 8.5. For FDK reconstructions, the experiments were performed on Intel(R) Xeon(R) CPU E5-1650 v3 at 3.7GHz RAM 32 and GPU 4GB memory. The shearlet-based method computation was performed on supercluster taito.csc.fi. ASTRA Toolbox and Spot operator were implemented [28, 31, 32]. All of the computations were set up using a cone beam geometry. The collection of projection images was downsampled with 3×3 binning to overcome computational challenges. For the sake of visualization, only one slice

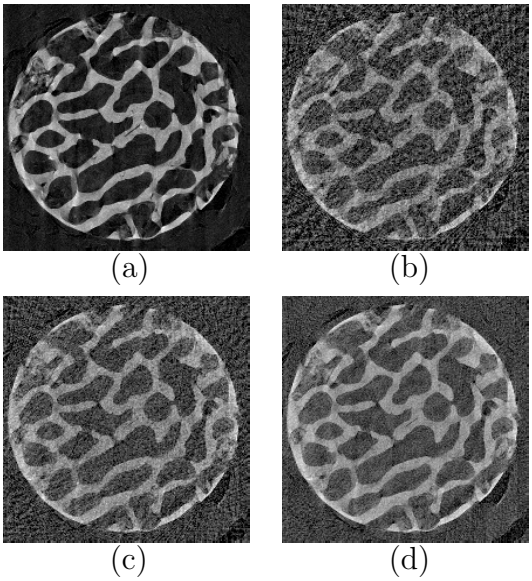

FIGURE 3. One slice of 3D reconstruction image of healthy bone (a) The ground truth (FDK reconstruction of the healthy bone from the full set 596 data). (b) reconstruction image using FDK from 40 projection images. (c) and (d) using 60 and 120 projection images, respectively.

of 3D-reconstructions using shearlet-based method and FDK are presented.

In details, the initial value for thresholding parameter μ^0 was calculated from the absolute mean of $(1-\mathcal{C}_{pr})$ of the shearlet coefficients from the backprojection reconstruction. The maximum number of iteration $I_0 = 500$.

We set the control step size $\beta = 100\mu^0$ and $\epsilon = 5 \times 10^{-3}$ as the stopping rule. Sixty five percent of nonzero coefficients were used for the *a priori* sparsity level ($\mathcal{C}_{pr}$). The shearlet-based reconstructions are shown in Figure 5 and Figure 9. The ROI of the reconstruction images were chosen and segmented by applying the steps in Subsection 2.5. The segmented images are shown in Figure 4, Figure 6, Figure 8 and Figure 10.

For comparison, FDK reconstructions of healthy and osteoarthritic bones were computed as well. It can be seen in Figure 3 and Figure 7. The segmented images of FDK reconstructions are presented in Figure 4 and Figure 8. The bone parameters for FDK and shearlet-based reconstructions are given in Table 4, Table 5, Table 6 and Table 7.

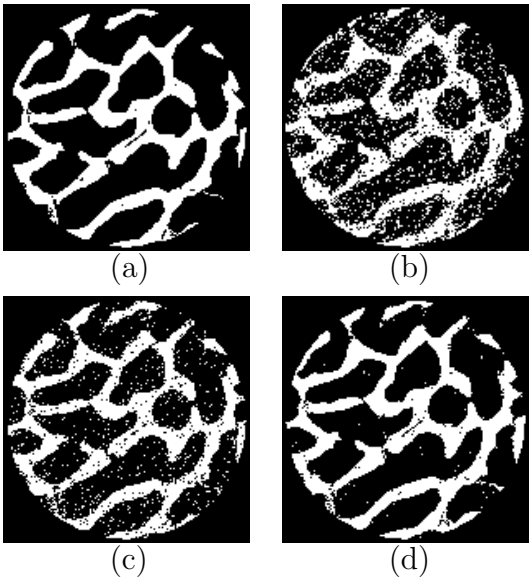

FIGURE 4. One slice of segmented image of healthy bone reconstructions (a) Segmented image of the ground truth. (b) Segmented image of 3D reconstruction using FDK from 40 projection images. (c) and (d) using 60 and 120 projection images, respectively.

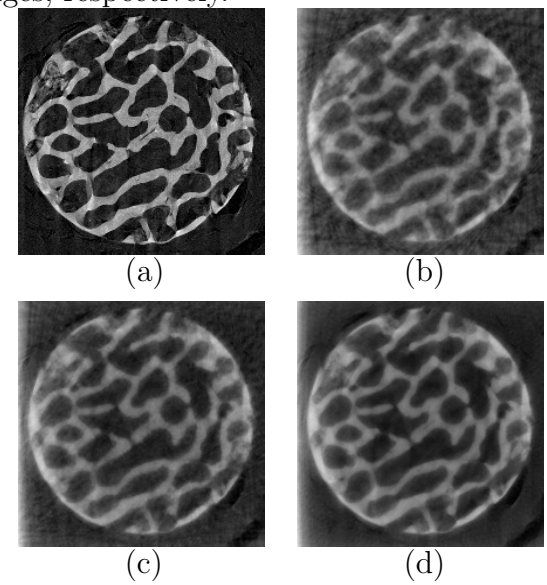

FIGURE 5. One slice of 3D reconstruction image of healthy bone (a) The ground truth (FDK reconstruction of the healthy bone from the full set 596 data). (b) reconstruction image using shearlet-based method from 40 projection images. (c) and (d) using 60 and 120 projection images, respectively.

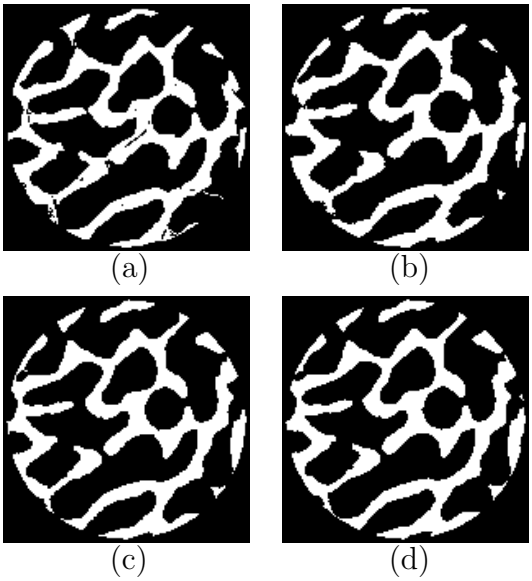

FIGURE 6. One slice of segmented image of healthy bone reconstructions (a) Segmented image of the ground truth. (b) Segmented image of 3D reconstruction using shearlet-based method from 40 projection images. (c) and (d) using 60 and 120 projection images, respectively.

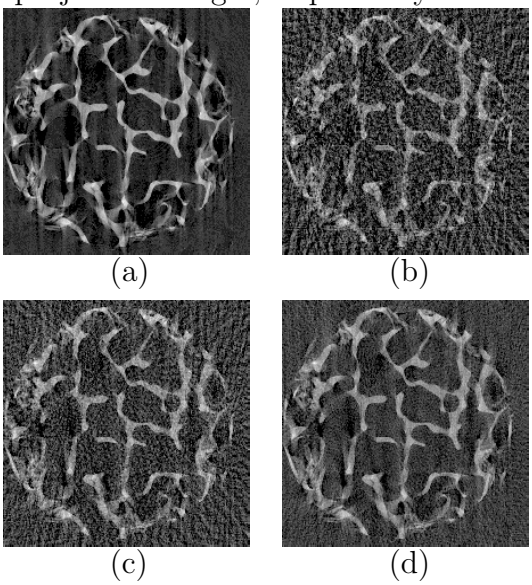

FIGURE 7. One slice of 3D reconstruction image of osteoarthritic bone (a) The ground truth (FDK reconstruction of the osteoarthritic bone from the full set 596 data). (b) reconstruction image using FDK from 40 projection images. (c) and (d) using 60 and 120 projection images, respectively.

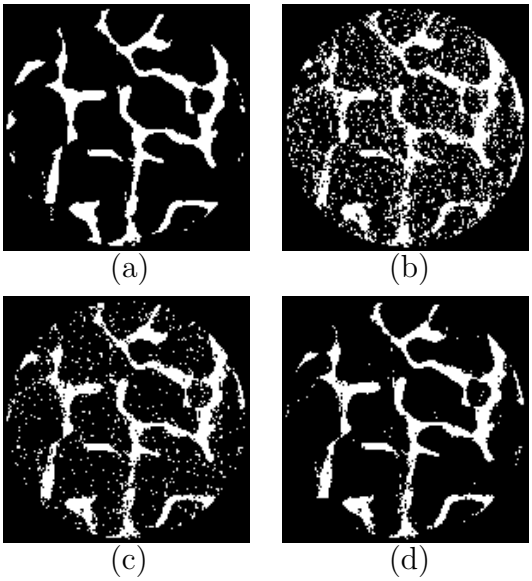

FIGURE 8. One slice of segmented image of osteoarthritic bone reconstructions (a) Segmented image of the ground truth. (b) Segmented image of 3D reconstruction using FDK from 40 projection images. (c) and (d) using 60 and 120 projection images, respectively.

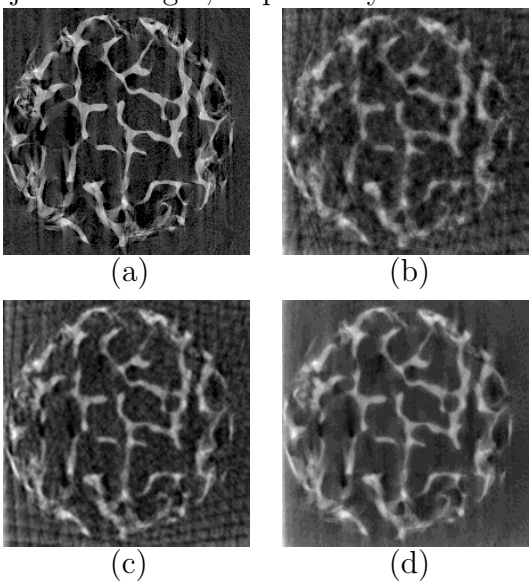

FIGURE 9. One slice of 3D reconstruction image of osteoarthritic bone (a) The ground truth (FDK reconstruction of the osteoarthritic bone from the full set 596 data). (b) reconstruction image using shearlet-based method from 40 projection images. (c) and (d) using 60 and 120 projection images, respectively.

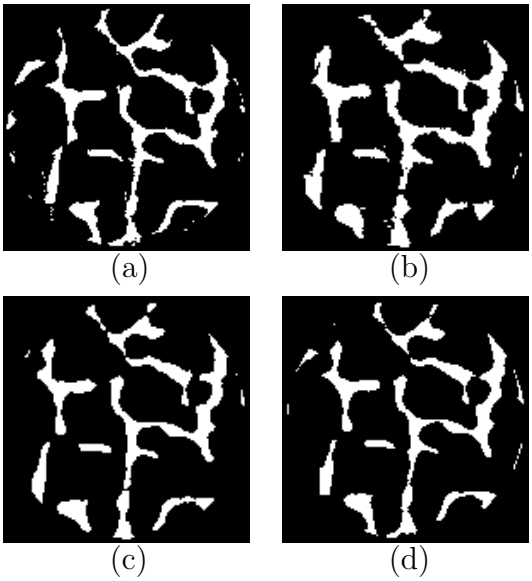

FIGURE 10. One slice of segmented image of osteoarthritic bone reconstructions (a) Segmented image of the ground truth. (b) Segmented image of 3D reconstruction using shearlet-based method from 40 projection images. (c) and (d) using 60 and 120 projection images, respectively.

TABLE 4. The bone morphometric parameters calculation for FDK reconstruction of healthy bone from different number of projection images.

Number of projections	*BV/TV*	*Tb.Th*	*Tb.N*	*Tb.Sp*
Ground truth: 596	41.0%	8.1	0.05	15.3
120	41.3%	6.5	0.06	9.7
60	41.7%	4.0	0.10	4.4
40	44.2%	3.4	0.13	3.3

TABLE 5. The bone morphometric parameters calculation for FDK reconstruction of osteoarthritic bone from different number of projection images.

Number of projections	*BV/TV*	*Tb.Th*	*Tb.N*	*Tb.Sp*
Ground truth: 596	19.0%	5.9	0.03	21.0
120	19.2%	5.3	0.04	14.0
60	21.5%	4.3	0.05	5.5
40	28.5%	2.5	0.08	3.7

TABLE 6. The bone morphometrics parameters for shearlet-based reconstruction of healthy bone from different projection data.

Number of projections	BV/TV	$Tb.Th$	$Tb.N$	$Tb.Sp$
Ground truth: 596	41.0%	8.1	0.05	15.3
120	41.3%	9.0	0.05	16.4
60	41.0%	8.9	0.05	16.2
40	40.9%	8.8	0.05	15.1

TABLE 7. The bone morphometrics parameters for shearlet-based reconstruction of osteoarthritic from different projection data.

Number of projections	BV/TV	$Tb.Th$	$Tb.N$	$Tb.Sp$
Ground truth: 596	19.0%	5.9	0.03	21.0
120	19.9%	6.5	0.03	21.6
60	21.0%	6.5	0.03	20.9
40	24.6%	7.2	0.03	18.5

TABLE 8. Computation times of FDK method (in seconds)

Number of projections	FDK for healthy and osteoarthritic bone
120	4.4
60	2.4
40	1.9

TABLE 9. Computation times of shearlet-based method for healthy and osteoarthritic bone (in seconds)

Number of projections images	shearlet-based method for healthy bone	shearlet -based method for osteoarthritic bone
120	15 395 (91 iterations)	12 168 (72 iterations)
60	18 750 (115 iterations)	41 580 (252 iterations)
40	18 962 (116 iterations)	25 020 (148 iterations)

4. Discussion and Conclusion

We have presented X-ray reconstructions of the inner structures of the healthy and osteoarthritic human trabecular bones in 3D using sparse projection images. Using sparse projection data is desired as it reduces the often long scan times and high ionizing radiation doses in μCT. While traditional methods such as FDK require dense projection images to produce good reconstructions, we propose shearlet-based method with automatic choosing regularization parameter for robust reconstruction for the incomplete sampled datasets.

When the number of projection images is reduced, the significant streaking artifacts caused by incomplete projection images and also beam hardening appear in the FDK reconstruction images. The artifacts induce relatively poor quality segmented images. In Figure 4 and Figure 8, many nonzero pixel values appear in the air-regions. In Table 4 and Table 5, it can be seen that the bone morphometric parameters of FDK reconstruction become progressively worse when the fewer projection images was used. In both tables, the trabecular number ($Tb.N$) increases, whereas the trabecular thickness ($Tb.Th$) and the separation ($Tb.Sp$) decrease dramatically.

On the other hand, the reconstructions of the shearlet-based method yielded less artifacts. Therefore, better results in the segmented images were obtained. There are no show of the nonzero pixels values in the air-regions. It can be seen in Figure 6 and Figure 10. As we can also see in Table 6 and Table 7, the bone morphometric parameters calculation for healthy and osteoarthritic bones using sparser projection images is relatively stable. The values of BV/TV, $Tb.Th$, $Tb.N$ and $Tb.Sp$ are closer to the values of the ground truth parameters. The results show that the shearlet-based approach using considerably sparse projection images outperforms the conventional FDK approach.

The computation times of the FDK and the shearlet using different number of projection images are shown in Table 9 and Table 8. The shearlet-based method were run with stopping rule criterion and it took around 72 - 252 iterations with different type of bone and different number of projection images. The computation time could be speed-up by implementing parallelized GPU code.

Acknowledgements

This work was supported by the Academy of Finland (Finnish Centre of Excellence in Inverse Problems Research 2012–2017, and grant nos. 268378 and 303786), and the European Research Council under the European Unions Seventh Framework Programme (FP/2007-2013)/ERC

Grant Agreement no. 336267. We warmly thank Tatiana Bubba for the discussion of the shearlet.

References

[1] L. Feldkamp, L. Davis, and J. Kress, "Practical cone-beam algorithm," JOSA A, vol. 1, no. 6, pp. 612–619, 1984.

[2] J. M. Boone, O. Velazquez, and S. R. Cherry, "Small-animal x-ray dose from micro-ct," Molecular imaging, vol. 3, no. 3, p. 15353500200404118, 2004.

[3] J. L. Mueller and S. Siltanen, Linear and nonlinear inverse problems with practical applications. Siam, 2012, vol. 10.

[4] S. Boutroy, M. L. Bouxsein, F. Munoz, and P. D. Delmas, "In vivo assessment of trabecular bone microarchitecture by high-resolution peripheral quantitative computed tomography," The Journal of Clinical Endocrinology & Metabolism, vol. 90, no. 12, pp. 6508–6515, 2005.

[5] L. A. Feldkamp, S. A. Goldstein, M. A. Parfitt, G. Jesion, and M. Kleerekoper, "The direct examination of three-dimensional bone architecture in vitro by computed tomography," Journal of bone and mineral research, vol. 4, no. 1, pp. 3–11, 1989.

[6] J. Kuhn, S. Goldstein, L. Feldkamp, R. Goulet, and G. Jesion, "Evaluation of a microcomputed tomography system to study trabecular bone structure," Journal of Orthopaedic Research, vol. 8, no. 6, pp. 833–842, 1990.

[7] P. Rüegsegger, B. Koller, and R. Müller, "A microtomographic system for the nondestructive evaluation of bone architecture," Calcified tissue international, vol. 58, no. 1, pp. 24–29, 1996.

[8] M. L. Bouxsein, S. K. Boyd, B. A. Christiansen, R. E. Guldberg, K. J. Jepsen, and R. Müller, "Guidelines for assessment of bone microstructure in rodents using micro–computed tomography," Journal of bone and mineral research, vol. 25, no. 7, pp. 1468–1486, 2010.

[9] A. Postnov, A. Vinogradov, D. Van Dyck, S. Saveliev, and N. De Clerck, "Quantitative analysis of bone mineral content by x-ray microtomography," Physiological measurement, vol. 24, no. 1, p. 165, 2003.

[10] M. A. Finnilä, J. Thevenot, O.-M. Aho, V. Tiitu, J. Rautiainen, S. Kauppinen, M. T. Nieminen, K. Pritzker, M. Valkealahti, P. Lehenkari et al., "Association between subchondral bone structure and osteoarthritis histopathological grade," Journal of Orthopaedic Research, 2016.

[11] G. Mohan, E. Perilli, J. S. Kuliwaba, J. M. Humphries, I. H. Parkinson, and N. L. Fazzalari, "Application of in vivo micro-computed tomography in the temporal characterisation of subchondral bone architecture in a rat model of low-dose monosodium iodoacetate-induced osteoarthritis," Arthritis research & therapy, vol. 13, no. 6, p. R210, 2011.

[12] N. Otsu, "A threshold selection method from gray-level histograms," Automatica, vol. 11, no. 285-296, pp. 23–27, 1975.

[13] G. Kutyniok and D. Labate, Shearlets: Multiscale analysis for multivariate data. Springer Science & Business Media, 2012.

[14] G. Kutyniok, W.-Q. Lim, and R. Reisenhofer, "Shearlab 3d: Faithful digital shearlet transforms based on compactly supported shearlets," ACM Transactions on Mathematical Software (TOMS), vol. 42, no. 1, p. 5, 2016.

[15] K. Guo and D. Labate, "Optimally sparse representations of 3d data with c^2 surface singularities using parseval frames of shearlets," SIAM Journal on Mathematical Analysis, vol. 44, no. 2, pp. 851–886, 2012. [Online]. Available: http://dx.doi.org/10.1137/100813397

[16] I. Loris and C. Verhoeven, "On a generalization of the iterative soft-thresholding algorithm for the case of non-separable penalty," Inverse Problems, vol. 27, no. 12, p. 125007, 2011.

[17] I. Daubechies, M. Defrise, and C. De Mol, "An iterative thresholding algorithm for linear inverse problems with a sparsity constraint," Communications on pure and applied mathematics, vol. 57, no. 11, pp. 1413–1457, 2004.

[18] K. J. Åström and T. Hägglund, "Pid controllers: theory, design, and tuning," 1995.

[19] F. Colonna, G. Easley, K. Guo, and D. Labate, "Radon transform inversion using the shearlet representation," Applied and Computational Harmonic Analysis, vol. 29, no. 2, pp. 232–250, 2010.

[20] B. Vandeghinste, B. Goossens, R. Van Holen, C. Vanhove, A. Pizurica, S. Vandenberghe, and S. Staelens, "Combined shearlet and tv regularization in sparse-view ct reconstruction," in 2nd International Meeting on image formation in X-ray Computed Tomography, 2012.

[21] E. Garduño and G. T. Herman, "Computerized tomography with total variation and with shearlets," arXiv preprint arXiv:1608.06668, 2016.

[22] T. Bubba, F. Porta, G. Zanghirati, and S. Bonettini, "The roi ct problem: a shearlet-based regularization approach," in Journal of Physics: Conference Series, vol. 756, no. 1. IOP Publishing, 2016, p. 012009.

[23] J. Frikel, "Sparse regularization in limited angle tomography," Applied and Computational Harmonic Analysis, vol. 34, no. 1, pp. 117–141, 2013.

[24] K. Batenburg and J. Sijbers, "Discrete tomography from micro-ct data: application to the mouse trabecular bone structure," in Medical Imaging. International Society for Optics and Photonics, 2006, pp. 614 240–614 240.

[25] K. J. Batenburg and J. Sijbers, "Dart: a practical reconstruction algorithm for discrete tomography," IEEE Transactions on Image Processing, vol. 20, no. 9, pp. 2542–2553, 2011.

[26] K. Guo and D. Labate, "Optimal recovery of 3d x-ray tomographic data via shearlet decomposition," Advances in Computational Mathematics, vol. 39, no. 2, pp. 227–255, 2013.

[27] G. H. Golub and C. F. Van Loan, Matrix computations. JHU Press, 2012, vol. 3.

[28] F. Bleichrodt, T. van Leeuwen, W. J. Palenstijn, W. van Aarle, J. Sijbers, and K. J. Batenburg, "Easy implementation of advanced tomography algorithms using the astra toolbox with spot operators," Numerical Algorithms, vol. 71, no. 3, pp. 673–697, 2016.

[29] K. Guo, G. Kutyniok, and D. Labate, "Sparse multidimensional representations using anisotropic dilation and shear operators," Wavelets und Splines (Athens, GA, 2005), G. Chen und MJ Lai, eds., Nashboro Press, Nashville, TN, pp. 189–201, 2006.

[30] D. Labate, W.-Q. Lim, G. Kutyniok, and G. Weiss, "Sparse multidimensional representation using shearlets," in Optics & Photonics 2005. International Society for Optics and Photonics, 2005, pp. 59 140U–59 140U.

[31] W. van Aarle, W. J. Palenstijn, J. Cant, E. Janssens, F. Bleichrodt, A. Dabravolski, J. De Beenhouwer, K. J. Batenburg, and J. Sijbers, "Fast and flexible x-ray tomography using the astra toolbox," Optics Express, vol. 24, no. 22, pp. 25 129–25 147, 2016.

[32] W. van Aarle, W. J. Palenstijn, J. De Beenhouwer, T. Altantzis, S. Bals, K. J. Batenburg, and J. Sijbers, "The astra toolbox: A platform for advanced algorithm development in electron tomography," Ultramicroscopy, vol. 157, pp. 35–47, 2015.